



## Communication

# Relaxation dynamics and thermodynamic properties of glassy Tb<sub>0.5</sub>Sr<sub>0.5</sub>MnO<sub>3</sub> single crystal

Hariharan Nhalil\*, Suja Elizabeth

Department of Physics, Indian Institute of Science, Bangalore 560012, India



## ARTICLE INFO

**Keywords:**  
Single crystal  
Spin-glass  
Memory effect

## ABSTRACT

Single crystals of Tb<sub>0.5</sub>Sr<sub>0.5</sub>MnO<sub>3</sub> were grown in an optical float zone furnace and their magnetic and thermodynamic properties were studied. Temperature dependent DC magnetization measurements at different fields show strong irreversibility below the magnetic anomaly at 44 K. The upward deviation from ideal CW behavior well above the transition temperature and its field independent nature are signatures of non-Griffiths phase. The origin non-Griffiths phase owe to competition between the antiferromagnetic and ferromagnetic Mn<sup>3+</sup>–Mn<sup>4+</sup> interactions mediated through intervening oxygen. Further, 44 K transition is confirmed as a magnetic glassy transition. The estimated dynamical spin flip time ( $\tau_0 = 2.11(3) \times 10^{-14}$  s) and  $z\nu(9.3(2))$  values fall into the range of typical spin-glass systems. Detailed memory and temperature cycling relaxation measurements were performed and support the Hierarchical relaxation model. Low-temperature specific heat data displays a linear term, identifying the glassy magnetic phase contribution.

## 1. Introduction

Doped rare earth manganites having general formula  $R_{1-x}A_x$  MnO<sub>3</sub> ( $R$ =rare earth,  $A$ =Ca, Ba, Sr) have been known to possess interesting magnetic and physical properties such as metal–insulator transition, magnetoresistance and charge ordering [1–3]. Generally, the terminal members ( $x=0$  and  $x=1$ ) are antiferromagnetic and insulating in nature. By replacing the rare earth ion ( $R^{3+}$ ) with divalent cation ( $A^{2+}$ ), one can generate multiple valencies for the Mn ion which, in turn, results in ferromagnetic (FM) double exchange interaction and antiferromagnetic (AFM) superexchange interaction between Mn<sup>3+</sup> and Mn<sup>4+</sup> ions [4,5]. The chemical pressure due to size mismatch and multiple valencies (Mn<sup>3+</sup>/Mn<sup>4+</sup>) can modify the Mn–O bond length and Mn–O–Mn bond angle, which causes structural distortion [6]. The magnetic phase in these compounds is primarily controlled by the amount of hole doping ( $x$ ), the average radius ( $\langle r_A \rangle$ ) of  $A$ -site cations and the variance ( $\sigma^2$ ) that determines the disorder due to random distribution of cations at the  $A$  site [7,8]. However,  $\sigma^2$  and  $\langle r_A \rangle$  have conflicting influence in determining the magnetic and transport properties [9]. For low value of  $\sigma^2$ , ferromagnetic metallic (FMM) state is preferred. As  $\sigma^2$  increases, charge ordered antiferromagnetic (CO-AFM) state is commonly stabilized [9]. Any further increase in  $\sigma^2$  results in an insulating spin-glass state [10]. If one analyzes  $\langle r_A \rangle$  dependence, especially for its large values, the FMM state is favored [11]. As  $\langle r_A \rangle$  decreases, FMM state transforms into CO-AFM, eventually

reverting to an insulating spin-glass state as in Nd<sub>0.5</sub>Sr<sub>0.5</sub>MnO<sub>3</sub> ( $\langle r_A \rangle = 1.236$  Å) and Y<sub>0.5</sub>Ca<sub>0.5</sub>MnO<sub>3</sub> ( $\langle r_A \rangle = 1.13$  Å) [11,12]. The impact of cationic size ( $\langle r_A \rangle$ ) is significant in charge ordering of manganites [7]. When  $\langle r_A \rangle$  is small ( $< 1.17$  Å), the charge ordered state is robust and not sensitive to the magnetic field [7].

The parent compound TbMnO<sub>3</sub> is a well-known type II multiferroic material [20]. It shows three magnetic transitions, each at 8 K, 27 K and 42 K. Below 27 K, the system is multiferroic. The choice of Sr as dopant at trivalent Tb site stems from the option of using a divalent cation of larger ionic radius and the prospect of exploring the extent of structural distortion and magnetic phases in Tb<sub>0.5</sub>Sr<sub>0.5</sub>MnO<sub>3</sub> (TSMO50) [13,14]. Here, single crystal growth and magnetic and thermal properties of Tb<sub>0.5</sub>Sr<sub>0.5</sub>MnO<sub>3</sub> crystals are discussed in detail.

## 2. Experiment

Single crystals of Tb<sub>0.5</sub>Sr<sub>0.5</sub>MnO<sub>3</sub> were grown by float zone technique using optical four mirror image furnace. Single crystallinity of the grown crystal was confirmed through X-ray Laue diffraction and phase purity was established by powder XRD patterns of crushed single crystal using a Philips X'pert X-ray diffractometer and Cu  $K\alpha$  radiation. DC magnetization data was obtained in a Magnetic Property Measurement System (Quantum Design Inc.). AC susceptibility studies were carried out under 170 mOe field and at four different frequencies between 9 Hz and 1000 Hz. Specific heat measurements were per-

\* Corresponding author.

E-mail addresses: [hariharan@physics.iisc.ernet.in](mailto:hariharan@physics.iisc.ernet.in), [hariharan.nhalil@gmail.com](mailto:hariharan.nhalil@gmail.com) (H. Nhalil).

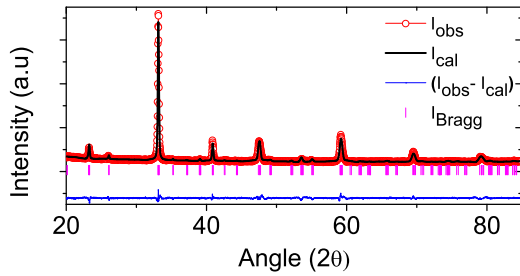


**Fig. 1.** (Color online) Powder XRD pattern of TSMO50 at room temperature. Rietveld refinement fit, difference pattern and Bragg positions are shown.

formed between 2 K and 300 K at 0 and 5 T fields.

### 3. Results and discussion

#### 3.1. Structure

Powder XRD data of the crushed single crystal shows no trace of impurities within the detection limit of the instrument. Data was refined by Rietveld [15] method in orthorhombic  $Pnma$  space group (space group no.=62) utilizing FULLPROF suite [16]. XRD pattern along with the refinement results is shown in Fig. 1. Refined lattice constants in  $Pnma$  settings are  $a=5.4023(7)$  Å,  $b=7.6641(2)$  Å, and  $c=5.3963(3)$  Å. These satisfy  $a \geq c \geq b/\sqrt{2}$  for O' type orthorhombic perovskite structure [17]. Detailed structural parameters are given in Table 1.

#### 3.2. XPS

In order to analyze the changes in Mn valency with  $\text{Sr}^{2+}$  doping, XPS data was analyzed. The Mn 2p spectra of TSMO50 are presented in Fig. 2 along with Gaussian fits assuming the presence of both  $\text{Mn}^{3+}$  and  $\text{Mn}^{4+}$ . The binding energies (BE) obtained from the analysis were 653.66 eV ( $\text{Mn } 2p_{1/2}$ ) and 641.92 eV ( $\text{Mn } 2p_{3/2}$ ). A faithful fit of the observed  $2p_{3/2}$  peak was obtained only by assuming mixed-valence for Mn. The peak positions of  $2p_{3/2}$  are compared with  $\text{MnO}_2$  and  $\text{Mn}_2\text{O}_3$  where Mn ion is in 4+ and 3+ valence states, respectively. The  $2p_{3/2}$  peak corresponding to  $\text{MnO}_2$  is observed at 642.6 eV ( $\text{Mn}^{4+}$ ), on the other hand, for  $\text{Mn}_2\text{O}_3$ , this peak is observed at 641.6 eV ( $\text{Mn}^{3+}$ ). In the present case, corresponding peaks are observed at 643.38 and 641.56 eV, close to the reported values of  $\text{Mn}^{4+}$  and  $\text{Mn}^{3+}$ . This suggests that in our case Mn is present in both 3+ and 4+ ionic states. An estimate of the ratio of  $\text{Mn}^{4+}$  and  $\text{Mn}^{3+}$  from the area under the Gaussian fitted curves is 0.97 which is close to the expected ratio 1 suggesting that approximately equal amount of  $\text{Mn}^{4+}$  and  $\text{Mn}^{3+}$  ions are present in TSMO50.

**Table 1**

Refined lattice parameters, bond angles, bond lengths and refinement fit agreement factor derived from the room temperature XRD data.

Space group	$Pnma$
$a$	5.4023(7) Å
$b$	7.6641(2) Å
$c$	5.3963(3) Å
Volume	223.427(1) Å <sup>3</sup>
$\langle \text{Mn-O-Mn} \rangle_{\text{Avr}}$	174.77(3)°
$\langle \text{Mn-O} \rangle_{\text{Avr}}$	1.837(4) Å
$\chi^2$	1.96
Tolerance factor ( $t$ )	0.9259(2)
$\sigma^2$	0.0121
$\langle r_A \rangle$	1.20 Å

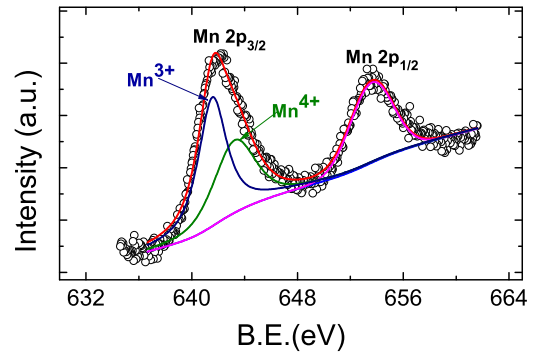


**Fig. 2.** (Color online) Mn 2p level XPS spectra of TSMO50. The graph also displays the Gaussian fitted curves assuming the presence of both  $\text{Mn}^{4+}$  and  $\text{Mn}^{3+}$ .

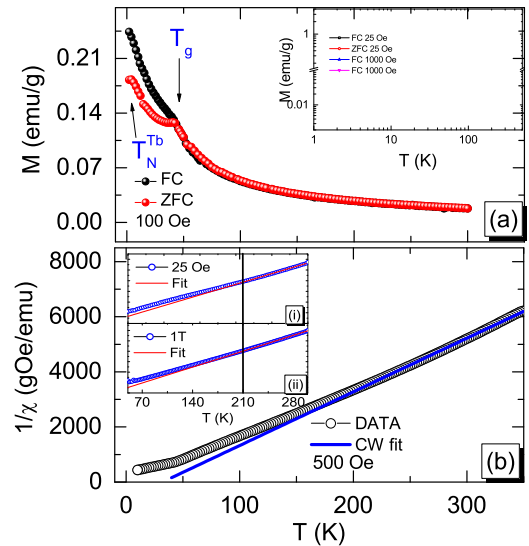


**Fig. 3.** (Color online) (a) Temperature dependent DC magnetization data at 100 Oe. The inset has plots at 25 Oe and 1000 Oe fields in log scale which show the decrease in bifurcation between FC and ZFC curves as the field increases. (b) Curie–Weiss fit in 230–350 K temperature range at 500 Oe. The inset shows the Curie–Weiss fit in the temperature range 230–300 K at (i) 25 Oe and (ii) 1 T fields.

#### 3.3. DC and AC magnetization

FC/ZFC magnetization plots at 100 Oe field are illustrated in Fig. 3(a). The inset shows the plots at 25 Oe and 1000 Oe in log scale. At all three fields, the FC and ZFC curves display a clear hump-like feature at 44 K and bifurcate just below 44 K. The irreversibility in the FC/ZFC data below a threshold temperature is likely due to the presence of a spin-glass state [18]. As shown in the inset of Fig. 3(a), the extent of bifurcation decreases as the field increases. This is seen in half doped manganites which show spin-glass magnetic properties [19]. Below 44 K, both FC and ZFC curves show a steady rise. A possible explanation for this behavior is the high paramagnetic response of  $\text{Tb}^{3+}$  ( $9.72 \mu_B$ ) moments. AFM ordering of Tb ions is reflected as a broad peak at 8 K in ZFC plot (marked as a  $T_N^{\text{Tb}}$  in Fig. 3(a)) [20].

The inverse susceptibility ( $1/\chi$ ) vs  $T$  plot at 500 Oe along with Curie–Weiss (CW) fit is illustrated in the main panel of Fig. 3(b). Curve fitting is done in the temperature range 230–350 K. The  $1/\chi$  plot deviates from a straight line below  $\sim 230$  K suggesting onset of magnetic ordering of Mn moments. The effective magnetic moment and CW temperature calculated from the fit are  $\mu_{\text{eff}}(E) = 7.75 \pm 0.06 \mu_B/\text{f. u.}$  and  $\theta = 42.39(5)$  K, respectively. A positive value of  $\theta$  is suggestive of dominant FM double exchange interaction over AFM superexchange interaction between Mn ions. Yoshii et al. [21] have observed similar behavior in polycrystalline TSMO50 but the

value of  $\theta$  reported was higher. Valance state of Mn is analyzed via XPS spectra and from the area under the curve of Mn 2p<sub>3/2</sub> peak almost equal amount of Mn<sup>3+</sup> and Mn<sup>4+</sup> is identified (Fig. 2). Paramagnetic effective moment is calculated using the formula  $\mu_{\text{eff}}(T) = \sqrt{0.5\mu_{\text{eff}}^2(\text{Tb}^{3+}) + 0.5\mu_{\text{eff}}^2(\text{Mn}^{3+}) + 0.5\mu_{\text{eff}}^2(\text{Mn}^{4+})}$ , by taking  $\mu_{\text{eff}}(\text{Tb}^{3+})=9.72 \mu_B$ ,  $\mu_{\text{eff}}(\text{Mn}^{3+})=4.9 \mu_B$  and  $\mu_{\text{eff}}(\text{Mn}^{4+})=3.87 \mu_B$  and is calculated as  $8.16 \mu_B/\text{f.u.}$  which is slightly higher than the experimental estimate,  $7.75 \mu_B/\text{f.u.}$

A deviation well above the transition temperature is discernible in Fig. 3(b) from the CW analysis. The downturn (–ve deviation) is typical of Griffiths phase (GP) [22], which corresponds to FM clusters in PM phase. An upturn (+ve deviation) is at variance to the GP model and is termed as non-Griffiths phase. An important difference between GP and non-GP is the field dependence [23,24]. In GP, the downturn behavior of  $1/\chi$  is suppressed with increasing external field due to polarization of spins outside the clusters; but, in non-GP, the upturn behavior is independent of field strength [24–26]. The inset of Fig. 3(b) shows the CW fit for two fields: (i) 25 Oe and (ii) 1 T. The fits deviate almost at the same temperature (230 K) at both fields reminiscent of field independent behavior and non-GP below 230 K. The non-GP nucleate due to competition between FM and AFM phases. Non-GP phase has been reported widely in compounds with FM-AFM competition such as manganites [25,26], cobaltites [24] and double perovskites [23]. It is likely that Mn<sup>3+</sup>–O–Mn<sup>3+</sup>, Mn<sup>3+</sup>–O–Mn<sup>4+</sup> and Mn<sup>4+</sup>–O–Mn<sup>4+</sup> interactions favor different types of magnetic order and competition between them make the system frustrated.

Fig. 4(a) shows the magnetic isotherm at 5 K. The magnetic field is varied between +140 kOe and –140 kOe. The right inset in Fig. 4(a) displaying the enlarged portion at low field levels exhibits a small hysteresis at 5 K. Even though CW analysis assumed FM interaction, prominent FM hysteresis was not seen in MH measurements. MH plots at different temperatures below 50 K (Fig. 4(b)) display weak hysteresis loop up to 40 K but none at 50 K. Magnetization is not saturated till 5 K even with applied field of 140 kOe; this result rules out long-range magnetic order. The maximum moment observed at 140 kOe is  $\sim 3.4 \mu_B/\text{f.u.}$  which is very low compared to the saturation moment ( $8.16 \mu_B/\text{f.u.}$ ). The coercive field observed at 5 K (inset of Fig. 4(b)) decreases as temperature increases and disappears above 44 K. The field dependence of magnetization clearly varies between 20 and 30 kOe and this slope change of MH curve is attributable to magnetic ordering and/or the crystal field effect due to Tb<sup>3+</sup> ions in rare earth containing perovskites.

Temperature variation of normalized real part of AC susceptibility at four different AC frequencies are illustrated in the main panel of Fig. 5. The inset (a) gives the imaginary components. Measurement was carried out under constant AC field of 170 mOe. A deviation from smooth curve is observed at about 44 K and the point of inflection

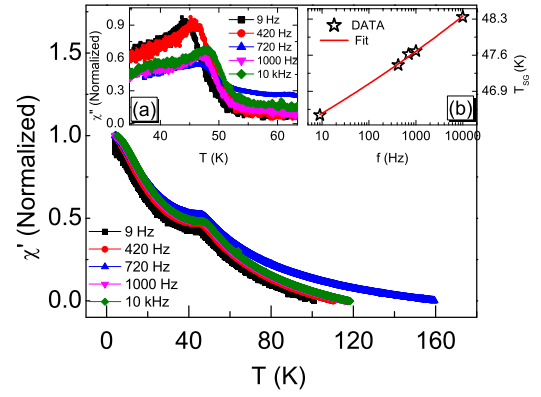


Fig. 5. (Color online) Temperature variation of real part of normalized AC susceptibility at different frequencies. The inset (a) gives the imaginary part and (b) the fit according to Eq. (1).

shifts to higher temperatures with increase in frequency (peak temperature is calculated by subtracting background from the imaginary part). This is a signature of glassy transition. Such behavior has been reported in compounds like Dy<sub>0.5</sub>Sr<sub>0.5</sub>MnO<sub>3</sub> and Gd<sub>0.5</sub>Sr<sub>0.5</sub>MnO<sub>3</sub> [19,27].

For a true spin-glass transition, the onset of glassy behavior at finite periodicity obeys critical scaling law near critical temperature  $T_c$  as described by the power law,

$$T_g(f) = T_c(1 + (\tau_0 f)^{1/\nu}) \quad (1)$$

where  $T_g$  is the glass transition temperature,  $\nu$  is the critical exponent and  $\tau_0$  is the characteristic spin flip time [28]. The experimental fit is shown in the inset (b) of Fig. 5 from which the fitting parameters  $\nu$  and  $\tau_0$  are estimated as 9.7(2) and  $4.11(5) \times 10^{-13}$  s, respectively. The critical spin glass temperature is ( $T_g$  at zero frequency)  $T_{cr}=44.22(3)$  K. For spin-glass systems, typical values of  $\tau_0$  and  $\nu$  are in the range of  $10^{-11}$ – $10^{-14}$  s and 4–12, respectively. Fitting parameters suggest true spin-glass phase below  $T_g$  in TSMO50. The relative shift of the spin freezing temperature can be empirically calculated as  $\delta T_g = \Delta T_g / T_g \Delta \log_{10} f$  and is estimated as 0.003. In this case  $\delta T_g$  is an indicator of frequency sensitivity, which implies that the sensitivity is comparable to canonical spin glass systems like CuMn ( $\delta T_g = 0.005$ ) [28]. Note that the total shift in  $T_g$  is approximately 2 K which is consistent with similar systems like Dy<sub>0.5</sub>Sr<sub>0.5</sub>MnO<sub>3</sub> [19].

### 3.4. Memory experiments and relaxation

#### 3.4.1. Memory experiments

Magnetic memory experiments were performed as per the follow-

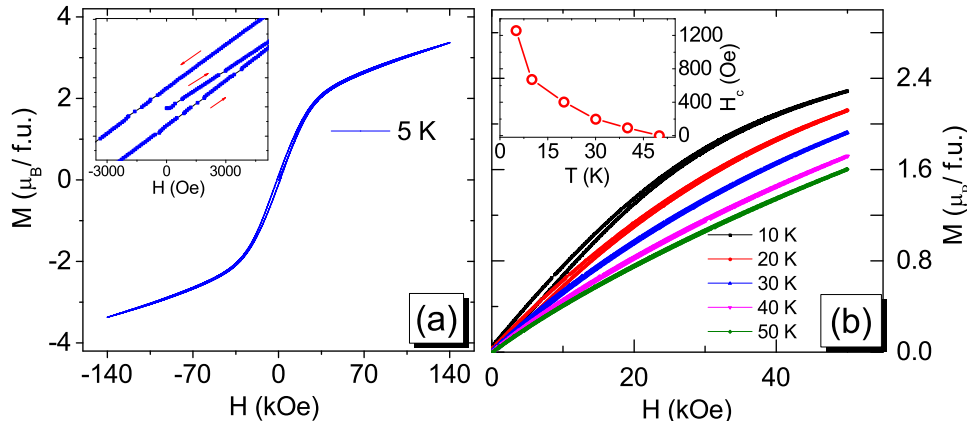
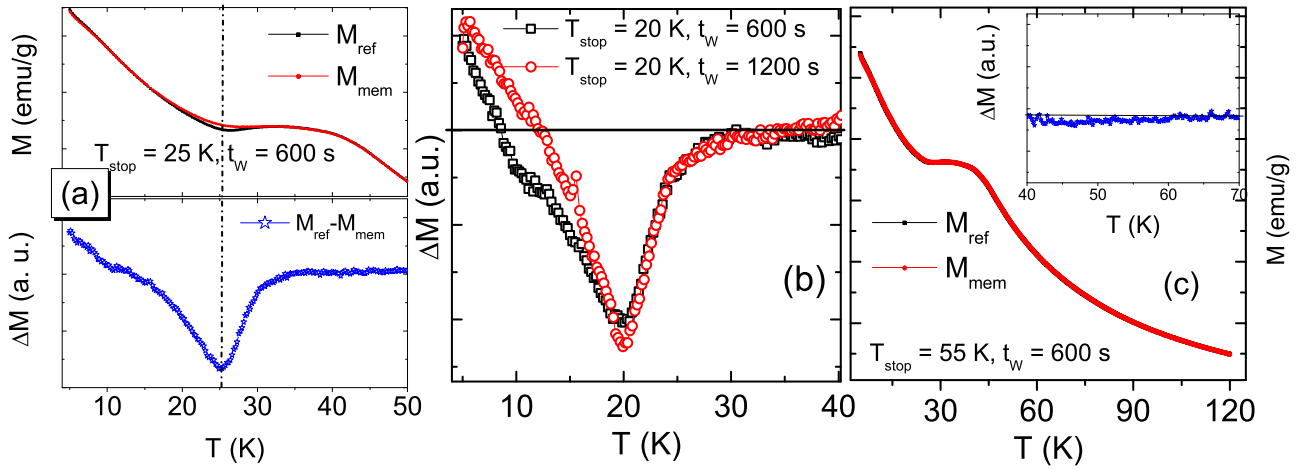


Fig. 4. (Color online) (a) Isothermal magnetization at fields between –140 kOe and +140 kOe at 5 K. The inset gives enlarged view of the 5 K plot to show the hysteresis. (b) MH plots at different temperatures and the inset shows the temperature dependence of coercive field ( $H_c$ ).



**Fig. 6.** (Color online) Results of memory experiment performed on TSMO50 single crystal according to the protocol given in the text. (a) Upper panel shows  $M_{ref}$  and  $M_{mem}$  and bottom panel displays the difference between the two. Here,  $T_{stop}$  and  $t_W$  are the stop temperature and waiting time, respectively. (b) Memory dips seen at 20 K for two different waiting periods ( $t_W$ ). (c)  $M_{ref}$  and  $M_{mem}$  and the difference (inset) for memory measurement at 55 K.

ing: The sample is cooled from 300 K to 5 K in zero field including a stop at an intermediate temperature ( $T_{stop}$ ) for  $t_W$  seconds. At 5 K, a magnetic field of 200 Oe is applied and the magnetization ( $M_{mem}$ ) measured as a function of temperature in the heating cycle. A regular ZFC measurement without waiting period at an intermediate temperature was also made for reference. The memory magnetization ( $M_{mem}$ ) curve with stop at intermediate temperature 25 K together with reference magnetization ( $M_{ref}$ ) are shown in upper panel of Fig. 6(a). The bottom part of (a) gives the difference curve ( $M_{ref} - M_{mem}$ ). A dip in memory is clearly seen at 25 K. During the waiting period, the system ages but the halt is remembered. Many A-site half doped spin-glass manganites and cobaltites have been reported with magnetic memory dips [29,30]. The present data confirm the slow dynamics and glassy nature of TSMO50. The experiment was again performed at low temperature of 20 K for two different  $t_W$  (10 and 20 min) and also at 55 K, which is above  $T_g$ . At 20 K, it is found that, with increase in  $t_W$ , the dip gets more steeper (Fig. 6(b)). This occurs because the system relaxes further with increase in waiting time. No memory dip is seen at 55 K (Fig. 6(c)).

### 3.4.2. Magnetic relaxation

A characteristic feature of glassy material below  $T_g$  is aging. To study the dynamics of the glassy state, ZFC magnetization relaxation measurements were performed using the following protocol: The sample was ZF cooled from well above  $T_g$  to the measuring temperature. Once the measurement temperature is reached, a field of 200 Oe is applied and the magnetization is recorded for 2 h as a function of time. The result of such relaxation measurements at 20 K and 15 K is plotted in Fig. 7(a). It is clear that the ZFC magnetization is not saturated even after two hours. In the glassy state, the moments are frozen in random direction and it takes a long time before they are aligned with the field direction. One of the most popular functional forms that was proposed to describe magnetization as a function of time is a stretched exponential expressed as,

$$M_r(H) = M_0(H) + [M_\infty(H) - M_0(H)]1 - \exp[-(t/t_0)^\alpha] \quad (2)$$

Here,  $t_0$  is the characteristic relaxation time and  $\alpha$  is the stretching parameter, which ranges between 0 and 1. Typical reference time ( $t_0$ ) is several orders of magnitude larger than the observed microscopic spin flip time,  $\tau_0$ .  $M_0$  and  $M_\infty$  are the magnetization at  $t=0$  and  $t=\infty$ , respectively. The best fit is obtained for  $M_\infty/M_0 = 1.03$  and 1.06,  $t_0=1518(3)$  s and 1650(4) s,  $\alpha=0.46(1)$  and 0.48(2) for  $T=20$  K and 15 K, respectively. It should be noted that the relaxation time  $t_0$ , i.e. the growth of magnetization, is slower at 15 K compared to that at 20 K. Generally, when the system is deep into the frozen state, magnetization

growth will slow down.

Metastable state of the TSMO50 was explored through isothermal remanent magnetization ( $M_{IRM}$ ) studies at two temperatures below  $T_g$ . The measurement protocol is as follows: the sample is cooled from paramagnetic phase to 20 K, a temperature below  $T_g$ . At this temperature, a field of 3 T is applied for 5 min. The field is switched off and the magnetization is recorded for one hour. The same measurement is performed at a lower temperature 15 K and both results are shown in Fig. 7(b). Decay of remanent magnetization slows significantly in the glassy state. It is observed that the decay is slower at 15 K than at 20 K. This is because the system goes deeper into the frozen state at 15 K than at 20 K. The decay occurs faster when the temperature gets closer to  $T_g$ .

$M_{IRM}$  relaxation data was fitted with the following equation [31]:

$$M_{IRM}(T, t) = M_{IRM}(T, 0) - S(T)\ln(1 + t) \quad (3)$$

where  $M_{IRM}(T, 0)$  and  $S(T)$  are the initial zero field remanent magnetization and magnetic viscosity, respectively. The fit (Eq. (3)) is also shown in Fig. 7(b). The best fit is obtained at  $M_{IRM}(T, 0)=0.85(1)$  emu/g and 0.62(1) emu/g,  $S=0.048(2)$  and 0.037(3) emu/g for 15 K and 20 K, respectively. It is found that both values decrease with increase in temperature. Magnetic viscosity corresponds to the time lag between the changes in magnetization in response to the changes in applied field. Logarithmic isothermal magnetization relaxation is observed in materials that display hysteric or spin-glass behavior. If the applied field is higher than the coercive field, the observed relaxation is attributable to spin-glass behavior [32,33]. Here, applied field is 3 T which is much higher than the coercive field. All these point to a glassy behavior.

### 3.4.3. Symmetry in temperature cycle

Memory and relaxation effects were further investigated through ZFC and FC relaxation experiments by -ve and +ve temperature cycling. The results are plotted in Figs. 8 and 9. In ZFC procedure, the sample was first zero-field-cooled from paramagnetic phase to the measuring temperature,  $T_1=25$  K. Subsequently, magnetic field of 200 Oe was applied and the magnetization recorded as function of time during the time period of  $t_1=40$  min. The sample was then quenched to lower temperature,  $T_2=15$  K without changing the field. Magnetization is now recorded for a time period of  $t_2=40$  min. Finally, the temperature was restored to  $T_3=25$  K and the magnetization was again recorded for the time period of  $t_3=40$  min. After quenching and halting at the lower temperature (15 K), magnetization is restored to the previous value before quenching (Fig. 8(a)). This indicates that a temporary quenching process does not erase memory in ZFC relaxa-

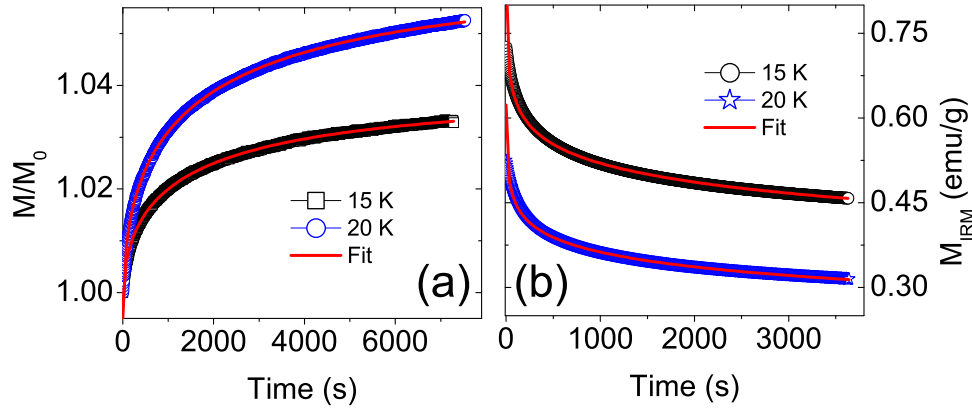


**Fig. 7.** (Color online) (a) ZFC magnetization relaxation (normalized with respect to the magnetization at  $t=0$ ) measured at  $T=15$  K and 20 K at  $H=200$  Oe. The solid lines represent the fits with the stretched exponential expression given in the text. (b) Isothermal remanent magnetization of TSMO50 at 15 and 20 K. The applied field is 30 kOe. Red solid lines are the fits according to Eq. (3).

tion. The magnetization data obtained during the aging periods  $t_1$  and  $t_3$  are plotted sequentially skipping the magnetization at  $t_2$ . These results are depicted in Fig. 8(b). The time spent at  $T_2$  appears completely ineffective, even though a large relaxation is observed during  $t_2$ . Magnetization recorded in the period  $t_3$  is in continuation to that recorded during  $t_1$ . This relates to a perfect memory effect by which the system remembers its initial configuration as it returns to the initial temperature after the temperature quench and relaxation. Such memory relaxation effects are observed in glassy systems [29].

A similar measurement was performed during FC cycle as well (Fig. 8(c)). The protocol is same as in the case of ZFC except that the sample was cooled under 200 Oe field and each time, the magnetization is recorded in the absence of field for 40 min. In both (ZFC and FC) methods, the relaxation curve during  $t_3$  is perceived to be an extension of the curve during  $t_1$  as shown in Figs. 8(b) and (d); this represents a clear memory effect.

#### 3.4.4. Asymmetry in temperature cycle:

Although the full understanding of the spin-glass nature is still open to debate, two theoretical models namely Droplet model [34,35] and

Hierarchical model [36,37] describe the spin glass magnetic state of a system fairly well. The Droplet model assumes symmetric behavior in magnetic relaxation with respect to heating and cooling. Whereas the Hierarchical model predicts that a positive temperature cycle may destroy the previous memory and re-initiate relaxation which means that the response is asymmetric. In order to gain deeper insight into the magnetic relaxation mechanism in TSMO50, measurements with intermittent heating cycles were performed in both ZFC and FC processes. The results are illustrated in Figs. 9(a) and (b) for ZFC cycle and Figs. 9(c) and (d) for the FC cycle. It can be seen that positive temperature cycling erases memory and reinitializes relaxation in both ZFC and FC processes. The behavior under intermittent temperature change during the relaxation experiments is in agreement with the Hierarchical model.

According to Hierarchical model, there exists a multi-valley free-energy surface for frustrated system at a given temperature  $T$ . Quenching the system from above  $T_g$  to  $T$  ( $T < T_g$ ) takes the system into the complicated free-energy landscape defined at  $T$ . When the system is allowed to relax at  $T$ , it tries to attain a quasi-equilibrium occupation rates among the other states. Upon cooling from  $T$  to

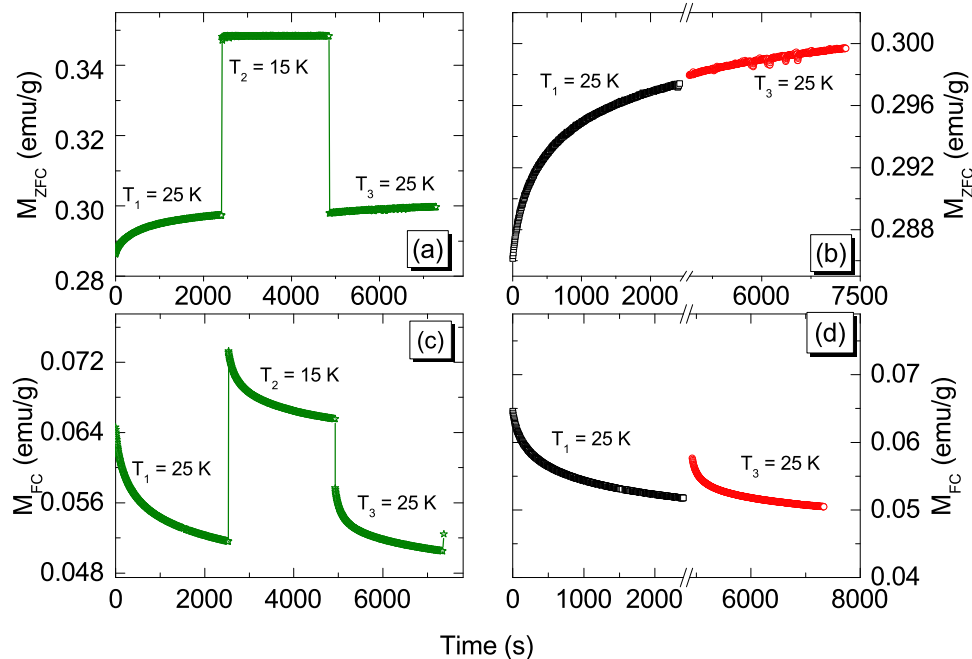


**Fig. 8.** (Color online) Magnetic relaxation in TSMO50 at 25 K with temporary quench to 15 K for ZFC (a, b) and FC (c, d) methods. In both cases, relaxation data during  $t_1$  and  $t_3$  merge almost perfectly as seen in (b) and (d) showing clear memory effect.



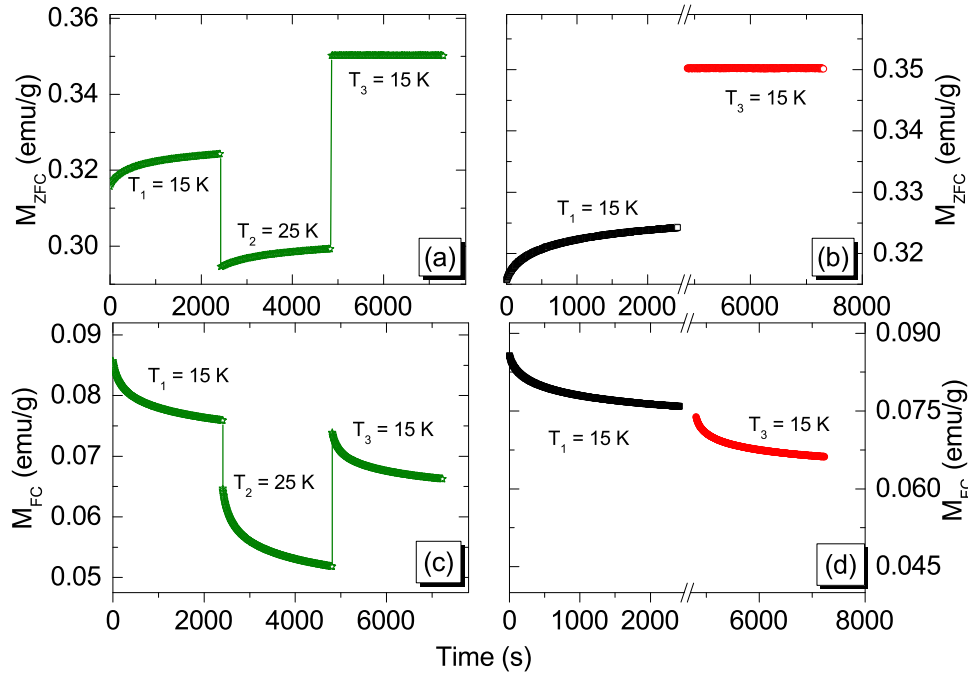


**Fig. 9.** (Color online) Asymmetry in the magnetic response to an intermittent heating cycle for ZFC (a, b) and FC (c, d) processes. In both cases, relaxation data during  $t_3$  do not follow the relaxation during  $t_1$  as seen in (b) and (d) which show that the memory has been erased by intermediate positive temperature cycling.

$T - \Delta T$ , the free energy valleys split into new sub-valleys. A large magnitude of  $\Delta T$  will form large barriers that separate the original valleys thus forcing the system to access states within the newly formed sub-valleys only. That is, as the system at  $T$  is cooled to  $T - \Delta T$ , it will confine itself to the newly formed states since the barriers separating it from other states are too high. During the time period  $t_2$ , it tries to attain a quasi-equilibrium occupation between the states within. When the system returns to its initial temperature  $T$ , the sub-valleys coalesce to the original free-energy surface and the relaxation at  $T$  resumes without being disturbed by the intermediate relaxations at  $T - \Delta T$ . However, the scenario is different when the system is heated from  $T$  to  $T + \Delta T$ . Here, the free energy barriers between the primary valleys (or states) are lower. Sometimes, these valleys merge with each other. During the time period  $t_2$ , relaxation can occur easily between primary valleys. When the temperature is restored to  $T$ , the original free energy surface is also regained. But the relative population or occupancy of each newly formed primary energy valley does not remain the same as before. A temporary heating cycle thus erases the memory effect. Behavior of this kind is observed in doped manganites, cobaltites, etc. [29,30].

### 3.5. Specific heat

Specific heat plot at zero field in the temperature range 2–300 K for TSMO50 is shown in Fig. 10. The measured values are in agreement with published data in other half doped manganites [19,38–40]. The limiting heat capacity at high temperature is ( $3rR$ -Dulong–Petit law)  $\sim 125$  J/mol K (in the present case  $r=5$ ), and the value measured at room temperature reaches up to  $\sim 95\%$  of this value. This means that the major contribution comes from the vibrational heat capacity. A very small feature at 44 K (shown by an arrow in the inset of Fig. 10) indicate spin glass transition. It is known that the spin glass anomaly is rarely visible in specific heat data.

The low temperature data between 2 K and 50 K has been successfully analyzed by considering different contributions. The total specific heat  $C_{tot}$  is given by,

$$C_{tot} = C_{latt} + C_{sg} + C_{Schot} \quad (4)$$

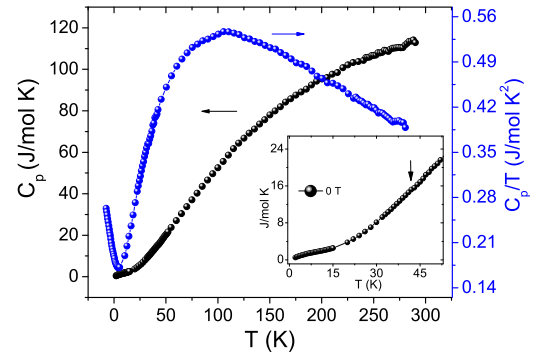


**Fig. 10.** (Color online) Temperature dependence of specific heat of  $\text{Tb}_{0.5}\text{Sr}_{0.5}\text{MnO}_3$ . The inset shows the enlarged plot to show the anomaly seen near spin-glass transition, which is marked by an arrow.

where  $C_{latt}$  is the lattice contribution,  $C_{sg}$  is the spin glass contribution and  $C_{Schot}$  is a two level system Schottky anomaly term. These are given as,

$$C_{latt} = B_3 T^3 + B_5 T^5 \quad (5)$$

$$C_{sg} = S T^n \quad (6)$$

$$C_{Schot} = R \left( \frac{\Delta}{k_B T} \right)^2 \frac{e^{\frac{\Delta}{k_B T}}}{[1 + e^{\frac{\Delta}{k_B T}}]^2} \quad (7)$$

Here,  $\Delta$  is the energy difference between two states,  $k_B$  is the Boltzmann constant and  $R$  is the universal gas constant. Since a linear specific heat contribution is expected for glassy magnetic systems, ' $n$ ' is taken as 1 in the Eq. (6) [19,28]. We did not consider the hyperfine contribution as it is significant only below 2 K. Considering the insulating behavior of the sample at low temperature, the linear free electronic contribution to the specific heat is also excluded. The fit according to Eq. (4) is shown in Fig. 11. The estimated fit parameters are  $B_3 = 1.96(2) \times 10^{-4}$  J mol $^{-1}$  K $^{-4}$ ,  $B_5 = -3.13(4) \times 10^{-8}$  J mol $^{-1}$  K $^{-6}$ , and  $S = 0.10(2)$  J mol $^{-1}$  K $^{-1}$ . The inset of Fig. 11 shows the specific heat data at 5 T field along with zero field data in the 15–50 K temperature range. There is no appreciable influence of applied field on specific heat

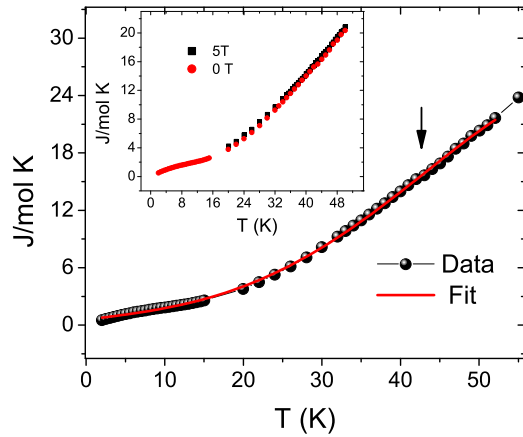


**Fig. 11.** (Color online) The main panel shows the specific heat data fit according to the model described in Eq. (4). The inset shows the specific heat at 0 and 5 T field in 15–50 temperature window.

in the measured temperature window.

The broad Schottky anomaly seen below 15 K is likely to originate from the magnetic ordering of  $Tb^{3+}$  ions. This is a result of split Kramers doublets of the 4f electrons. The Debye temperature is calculated from the lattice share of specific heat according to the following equation [41]:

$$\theta_D = \left( \frac{12\pi^4 R}{5B_3} \right)^{1/3} \quad (8)$$

where  $R$  is the universal gas constant and  $r$  is the number of atoms in the unit cell. The estimates  $\theta_D = 367.12(3)$  K was estimated is in fair agreement with the reported values on similar systems [19,42,43].

#### 4. Summary

In summary, single crystals of  $Tb_{0.5}Sr_{0.5}MnO_3$  were grown by float zone technique which are found to crystallize in the orthorhombic  $Pnma$  space group. DC magnetic measurements reveal a magnetic anomaly at  $\sim 44$  K which is corroborated as glassy magnetic transition. +ve CW temperature indicates that double exchange mediated FM interactions are preferred over the superexchange mediated AFM interactions in the material. The upturn from ideal CW behavior well above the transition temperature and its field independent nature are reminiscent of non-Griffiths phase. Competition between AFM and FM order is likely to be the origin of non-Griffiths phase. Magnetic moments are not saturated at 5 K even under applied field of 140 kOe, which excludes the possibility of long-range order. Irreversibility of temperature dependent magnetization, unsaturated magnetic isotherms at low temperature and high fields, AC magnetic susceptibility data and memory effects are all strong evidences for glassy dynamics in TSMO50. Temperature cycling relaxations results conform to the Hierarchical model. Large A-site cationic size mismatch together with mixed valency of Mn ions lead to magnetic frustration and glassy phase. Specific heat shows no sharp transition near the magnetic anomaly conforming the spin glass transition and a linear contribution to the total specific heat from the glassy magnetic phase

has been identified.

#### References

- [1] H. Kawano, R. Kajimoto, H. Yoshizawa, Y. Tomioka, H. Kuwahara, Y. Tokura, *Phys. Rev. Lett.* 78 (1997) 4253.
- [2] L.P. Gor'kov, V.Z. Kresin, *Phys. Rep.* 400 (2004) 149–208.
- [3] J. Coey, M.v. Viret, S. Von Molnar, *Adv. Phys.* 58 (2009) 571–697.
- [4] C. Zener, *Phys. Lett.* 82 (1951) 403.
- [5] T. Kimura, S. Ishihara, H. Shintani, T. Arima, K.T. Takahashi, K. Ishizaka, Y. Tokura, *Phys. Rev. B* 68 (2003) 060403.
- [6] M. Uehara, S. Mori, C. Chen, S. Cheong, *Nature* 399 (1999).
- [7] A. Arulraj, P.N. Santhosh, R.S. Gopalan, A. Guha, A.K. Raychaudhuri, N. Kumar, C.N.R. Rao, *J. Phys.: Condens. Matter* 10 (1998) 8497.
- [8] L.M. Rodriguez-Martinez, J.P. Attfield, *Phys. Rev. B* 54 (1996) R15622.
- [9] Y. Tokura, *Rep. Prog. Phys.* 69 (2006) 797.
- [10] A. Sundaresan, A. Maignan, B. Raveau, *Phys. Rev. B* 56 (1997) 5092.
- [11] R. Mahesh, R. Mahendiran, A.K. Raychaudhuri, C.N.R. Rao, *J. Solid State Chem.* 120 (1995) 204–207.
- [12] A. Arulraj, R. Gundakaram, A. Biswas, N. Gayathri, A.K. Raychaudhuri, C.N.R. Rao, *J. Phys.: Condens. Matter* 10 (1998) 4447.
- [13] M. Staruch, M. Jain, *J. Phys.: Condens. Matter* 25 (2013) 296005.
- [14] C.C. Wang, Y.M. Cui, L.W. Zhang, *Appl. Phys. Lett.* 90 (2007) 012904.
- [15] H.M. Rietveld, *J. Appl. Crystallogr.* 2 (1969) 65–71.
- [16] Juan Rodríguez-Carvajal, *Physica B: Condens. Matter* 192 (1993) 55–69.
- [17] P.M. Woodward, T. Vogt, D.E. Cox, A. Arulraj, C.N.R. Rao, P. Karen, A.K. Cheetham, *Chem. Mater.* 10 (1998) 3652–3665.
- [18] P.S.A. Kumar, P.A. Joy, S. Date, *J. Phys.: Condens. Matter* 10 (1998) L487.
- [19] S. Harikrishnan, C.N. Kumar, H. Bhat, S. Elizabeth, U. Röfller, K. Dörr, S. Röfller, S. Wirth, *J. Phys.: Condens. Matter* 20 (2008) 275234.
- [20] T. Kimura, T. Goto, H. Shintani, K. Ishizaka, T. Arima, Y. Tokura, *Nature* 426 (2003) 55–58.
- [21] K. Yoshii, Y. Hiramitsu, Y. Okajima, Y. Yoneda, Y. Nishihata, J. Mizuki, A. Nakamura, Y. Shimojo, Y. Ishii, Y. Morii, et al., *Mater. Res. Bull.* 45 (2010) 1574–1580.
- [22] R.B. Griffiths, *Phys. Rev. Lett.* 23 (1969) 17.
- [23] S.M. Zhou, Y.Q. Guo, J.Y. Zhao, S.Y. Zhao, L. Shi, *Appl. Phys. Lett.* 96 (2010) 262507.
- [24] C. He, M.A. Torija, J. Wu, J.W. Lynn, H. Zheng, J.F. Mitchell, C. Leighton, *Phys. Rev. B* 76 (2007) 014401.
- [25] S. Zhou, Y. Guo, J. Zhao, L. He, L. Shi, *J. Phys. Chem. C* 115 (2011) 1535–1540.
- [26] M.M. Saber, M. Egilmez, A.I. Mansour, I. Fan, K.H. Chow, J. Jung, *Phys. Rev. B* 82 (2010) 172401.
- [27] A.A. Wagh, P.S.A. Kumar, H.L. Bhat, S. Elizabeth, *J. Supercond. Nov. Magn.* 24 (2011) 665–667.
- [28] J.A. Mydosh, *Spin Glass: An Experimental introduction*, Taylor and Francis, London, 1999.
- [29] S. Harikrishnan, S. Röfller, C.M.N. Kumar, Y. Xiao, H. Bhat, U.K. Röfller, F. Steglich, S. Wirth, S. Elizabeth, *J. Phys.: Condens. Matter* 22 (2010) 346002.
- [30] Yk. Tang, Y. Sun, Zh. Cheng, *Phys. Rev. B* 73 (2006) 012409.
- [31] C.N. Guy, *J. Phys. F: Metal Phys.* 8 (1978) 1309.
- [32] K. Binder, A.P. Young, *Rev. Mod. Phys.* 58 (1986) 801.
- [33] L. Folks, R. Street, *J. Appl. Phys.* 76 (1994) 6391–6395.
- [34] D.S. Fisher, D.A. Huse, *Phys. Rev. B* 38 (1988) 386.
- [35] D.S. Fisher, D.A. Huse, *Phys. Rev. B* 38 (1988) 373.
- [36] Y. Sun, M.B. Salamon, K. Garnier, R.S. Averback, *Phys. Rev. Lett.* 91 (2003) 167206.
- [37] F. Lefloch, J. Hammann, M. Ocio, E. Vincent, *Europhys. Lett.* 18 (1992) 647.
- [38] A.K. Raychaudhuri, A. Guha, I. Das, R. Rawat, C.N.R. Rao, *Phys. Rev. B* 64 (2001) 165111.
- [39] J. López, O.F. de Lima, P.N. Lisboa-Filho, F.M. Araujo-Moreira, *Phys. Rev. B* 66 (2002) 214402.
- [40] A.G. Gamzatov, A.M. Aliev, A.B. Batdalov, H. Ahmadvand, H. Salamati, P. Kameli, *J. Mater. Sci.* 49 (2014) 294–299.
- [41] Charles Kittel, *Introduction to Solid State Physics*, Wiley, New York, 1996.
- [42] J.J. Hamilton, E.L. Keatley, H.L. Ju, A.K. Raychaudhuri, V.N. Smolyaninova, R.L. Greene, *Phys. Rev. B* 54 (1996) 14926.
- [43] M.R. Lees, O.A. Petrenko, G. Balakrishnan, D.M. Paul, *Phys. Rev. B* 59 (1999) 1298.